JAMES | Journal of Advances in Modeling Earth Systems

RESEARCH ARTICLE
10.1029/2020MS002179

Changes to the Madden-Julian Oscillation in Coupled and Uncoupled Aquaplanet Simulations With 4xCO_2

Hien X. Bui[1] and **Eric D. Maloney**[1]

[1]Department of Atmospheric Science, Colorado State University, Fort Collins, CO, USA

Key Points:
- Increased CO_2 concentrations produce only small changes in MJO characteristics when surface temperature is held fixed
- Coupled and uncoupled experiments exhibit different changes in MJO behavior with warming, even for the same climatological SST
- MJO propagation speed increases are greater in the coupled simulation with warming, possibly due to a different zonal wind basic state

Supporting Information:
- Supporting Information S1

Correspondence to:
H. X. Bui,
hien.bui@colostate.edu

Citation:
Bui, H. X., Maloney, E. D. (2020). Changes to the Madden-Julian Oscillation in coupled and uncoupled aquaplanet simulations with 4xCO_2. *Journal of Advances in Modeling Earth Systems*, *12*, e2020MS002179. https://doi.org/10.1029/2020MS002179

Received 10 MAY 2020
Accepted 3 JUL 2020
Accepted article online 8 JUL 2020

Abstract The impacts of rising carbon dioxide (CO_2) concentration and ocean feedbacks on the Madden-Julian Oscillation (MJO) are investigated with the Community Atmospheric Model Version 5 (CAM5) in an idealized aquaplanet configuration. The climate response associated with quadrupled CO_2 concentrations and sea surface temperature (SST) warming are examined in both the uncoupled CAM5 and a version coupled to a slab ocean model. Increasing CO_2 concentrations while holding SST fixed produces only small impacts to MJO characteristics, while the SST change resulting from increased CO_2 concentrations produces a significant increase in MJO precipitation anomaly amplitude but smaller increase in MJO circulation anomaly amplitude, consistent with previous studies. MJO propagation speed increases in both coupled simulations with quadrupling of CO_2 and uncoupled simulations with the same climatological surface temperature warming imposed, although propagation speed is increased more with coupling. While climatological SST changes are identical between coupled and uncoupled runs, other aspects of the basic state such as zonal winds do not change identically. For example, climate warming produces stronger superrotation and weaker mean lower tropospheric easterlies in the coupled run, which contributes to greater increases in MJO eastward propagation speed with warming through its effect on moisture advection. The column process, representing the sum of vertical moist static energy (MSE) advection and radiative heating anomalies, also supports faster eastward propagation with warming in the coupled run. How differing basic states between coupled and uncoupled runs contribute to this behavior is discussed in more detail.

Plain Language Summary Previous studies have suggested that the Madden-Julian Oscillation (MJO) will speed up under global warming. Understanding the MJO's response to rising carbon dioxide (CO_2) concentrations is complicated by the need to separate the direct response to CO_2 forcing from that associated with increasing temperatures. Ocean coupling may also mediate the MJO's response to warming. We demonstrate using the Community Atmospheric Model Version 5 (CAM5) run in an aquaplanet configuration that increasing CO_2 concentrations in isolation from temperature changes has only small impacts on MJO characteristics. However, the temperature changes resulting from a quadrupling of CO_2 produce a significant increase in the MJO precipitation amplitude but weaker increase in MJO wind amplitude. Even for the same climatological surface temperature increases, ocean coupling produces greater increases in eastward MJO propagation speed than in the uncoupled model. This is likely because other aspects of the model climate such as mean east-west winds change differently between coupled and uncoupled models. The model winds become more westerly in the coupled versus uncoupled model for the same surface temperature warming, which causes the MJO to speed up more in the coupled run. Other processes responsible for the more rapid eastward propagation of the MJO with warming in the coupled run are diagnosed.

1. Introduction

In this modeling study, changes of Madden-Julian Oscillation (MJO; Madden & Julian, 1971, 1972) propagation and amplitude in a CO_2-warmed climate are examined. Slow eastward propagation of the MJO at a speed of 5 m s^{-1} is observed over the tropical Indian Ocean and western Pacific during boreal winter and is one of the most fundamental features that distinguishes the MJO from other tropical phenomena (e.g., Wang et al., 2019; Zhang, 2005). The MJO has been observed to influence the onset of the global monsoon systems (Grimm, 2019; Marshall & Hendon, 2015; Wheeler et al., 2009) and modulate tropical cyclones in the eastern and western Pacific (e.g., Maloney & Hartmann, 2000; Sobel & Maloney, 2000), Atlantic

(Klotzbach & Oliver, 2015) and Indian ocean (e.g., Bessafi & Wheeler, 2006). The MJO also interacts with El Niño–Southern Oscillation (ENSO, Zhang & Gottschalck, 2002) and creates teleconnections and blocking in high latitudes (Henderson et al., 2016, 2017), among other phenomena. Hence, successful prediction of the MJO in weather forecasting and climate models is important for subseasonal prediction of many extreme weather phenomena (e.g., Vitart, 2009, 2014). Given these acute impacts of the MJO on weather and climate, an increasing body of work has been devoted to understanding how the MJO might change with anthropogenic warming (see Maloney et al., 2019, for a review).

Most studies project that MJO propagation speed will increase with global warming. Using the superparameterized Community Atmospheric Model (SP-CAM) with different sea surface temperature (SST) states, Arnold et al. (2013) showed an increase of MJO phase speed and a shift of the MJO spectrum toward higher frequencies as SST increased. Chang et al. (2015) also showed an increase in the frequency of the MJO with warming in the fifth generation of atmospheric general circulation model ECHAM (European Centre for Medium-Range Weather Forecasts model using a parameterization package developed in Hamburg) coupled to the one-column turbulent kinetic energy ocean model Snow-Ice-Thermocline (SIT) (ECHAM5-SIT). Adames et al. (2017) attributed the increase in MJO phase speed with climate warming in the National Aeronautics and Space Administration (NASA) Goddard Institute of Space Studies (GISS) model to enhanced horizontal moisture advection associated with an increased mean meridional moisture gradient and increase in the MJO's spatial scale. Similar results were found in an analysis of several Coupled Model Intercomparison Project Phase 5 (CMIP5) models with good MJO performance forced by Representative Concentration Pathway (RCP) 8.5 (Rushley et al., 2019). Recently, Cui and Li (2019) hypothesized that increased static stability contributes to the increased eastward phase speed of the MJO with warming through acceleration of equatorial Kelvin wave speed.

For MJO amplitude, many global climate models (GCMs) project enhanced amplitude of MJO precipitation at the end of 21st century (e.g., Maloney et al., 2019). The increased lower tropospheric moisture gradient appears to contribute to increases in MJO precipitation amplitude, although a more top-heavy MJO diabatic heating profile with warming opposes this tendency to some degree (Bui & Maloney, 2019a; Wolding et al., 2017). Changes in MJO circulation strength under anthropogenic warming have been shown to increase at a slower rate than precipitation or weaken due to the increases of static stability with surface warming (Bui & Maloney, 2018, and references therein). In general, the response of MJO amplitude to global warming is uncertain and highly dependent on which variable and time period is being considered. Bui and Maloney (2019a) reported a reduction in MJO precipitation amplitude in the early and middle 21st century in several CMIP5 models in RCP8.5 relative to the historical period, which they hypothesized might have a component due to the direct response of the MJO to greenhouse gas forcing rather than to changes in the thermodynamic environment that lag the forcing. Bui and Maloney (2019b) later analyzed 11 CMIP5 simulations including multiple ensemble members from one model to show that individual changes in MJO precipitation and circulation amplitude in RCP8.5 are not detectable until the last decades of the 21st century, casting doubt on the early 21st century findings of Bui and Maloney (2019a). Despite inability to detect individual changes of MJO precipitation and circulation amplitude, decreases in the ratio of MJO circulation to precipitation anomaly amplitude were detectable as early as the first half of the 21st century, consistent with increased tropical static stability produced by global mean temperature warming (e.g., Maloney & Xie, 2013). The studies above assessed simulations where the direct radiative effects of CO_2 forcing and increasing surface temperatures produced by that forcing were not separated in the context of their effect on the MJO. However, it has been previously shown that increased CO_2 can directly impact the tropical hydrologic cycle through fast adjustments independent of surface temperature changes (Gregory & Webb, 2008; Mitchell, 1983). These adjustments can increase atmospheric stability, reduce convection, and lead to a general reduction in tropical precipitation (e.g., Bony et al., 2013; Yang et al., 2003). These previous results highlighting the direct effect of greenhouse gas changes motivate us to test the relative influence of increased CO_2 concentrations in isolation from surface warming on MJO characteristics.

How the MJO response to warming depends upon ocean feedbacks is another open question. Several studies have argued that SST-driven surface flux feedbacks are important for maintenance and propagation of the MJO (Araligidad & Maloney, 2008; Riley Dellaripa & Maloney, 2015; Sobel et al., 2008). Warm SST anomalies that lead positive MJO precipitation anomalies are produced by suppressed surface heat flux and

reductions in mixed layer depth associated with reduced wind stress and surface buoyancy fluxes (Waliser et al., 2003). Some models have shown that coupling between the atmosphere and the ocean produces an approximate 20% increase in the amplitude of intraseasonal variability (e.g., Maloney & Sobel, 2004) and improves the model's ability to simulate the periodicity and organization of MJO convection (e.g., Kim et al., 2009). Coupling also modulates MJO surface fluxes, thus affecting MJO maintenance and propagation (DeMott et al., 2014, 2015, 2019; Klingaman & Woolnough, 2014). However, other studies show that air-sea interaction has only a small or even negative effect on MJO amplitude (e.g., Fu et al., 2015, 2017; Hendon, 2000).

To properly assess the role of ocean coupling to the MJO, mean state differences between coupled and uncoupled simulations that themselves affect the MJO need to be minimized (e.g., Klingaman & Woolnough, 2014). To do this, recent studies have prescribed the climatological mean SST from coupled simulations to the respective uncoupled model (e.g., DeMott et al., 2019, and references therein). Once mean state SST differences between coupled and uncoupled simulations are eliminated, coupling has been shown to increase mean state column water vapor near the equator, sharpening meridional moisture gradients and enhancing meridional moisture advection and MJO propagation speed (DeMott et al., 2019). However, the effect of coupling on MJO propagation speed in climate warming scenarios has not been examined by these studies or others to our knowledge.

Here, we will use moisture mode theory (e.g., Raymond & Fuchs, 2009; Sobel & Maloney, 2013) to help explain why MJO propagation changes in a future warmer climate. In moisture mode theory, intraseasonal convection propagates eastward because moistening occurs to the east of the MJO convective center and drying occurs to the west, which creates favorable conditions for eastward movement of convection (Sobel & Maloney, 2013). Maloney (2009) used a GCM to show that horizontal advection causes increases of moist static energy (MSE) within regions of anomalous equatorial lower tropospheric easterly anomalies, and drying in anomalous westerlies, which favor eastward propagation of the MJO. Maloney et al. (2010) also derived a similar conclusion in their aquaplanet simulations across different SST patterns. Andersen and Kuang (2012) performed aquaplanet simulations with SP-CAM and found that horizontal MSE advection played a key role in the propagation of the MJO-like disturbance. This finding has been supported by numerous other studies both in observations and models (e.g., Gonzalez & Jiang, 2017; Kim et al., 2014). Maloney (2009) found that the meridional component of moisture advection dominates the anomalous MJO MSE budget in the lower troposphere. Jiang (2017) decomposed the horizontal MSE advection term into different time scales and argued that the MJO anomalous circulation acting on the mean lower tropospheric meridional moisture gradient plays a critical role for the eastward propagation. The importance of the mean lower tropospheric moisture pattern to MJO propagation was also highlighted by Gonzalez and Jiang (2017), who showed that GCMs that underestimate the amplitude of the mean low-level moisture gradient produce unrealistic MJO propagation.

In this study, in addition to providing another datapoint on how general characteristics of the MJO are expected to change with global warming, we aim to (1) quantify how much the MJO change in a warming climate depends directly on higher CO_2 concentrations versus surface warming and (2) investigate how MJO propagation speed and amplitude changes in a warmer climate depend on ocean coupling. We address these questions by running a series of coupled (slab ocean) and uncoupled aquaplanet simulations in which the atmospheric CO_2 concentration is abruptly quadrupled and then held fixed to isolate the respective roles of CO_2 increases versus surface warming increases on MJO characteristics. These are aided by uncoupled runs in which only surface temperature increases are implemented. The aquaplanet is a simple form of a GCM where the lower boundary condition is simplified to that of a water covered surface while the full atmospheric model physics are retained (Blackburn & Hoskins, 2013). Aquaplanets forced by idealized SST patterns simplify model behavior and have been used extensively to understand the general circulation and processes underlying tropical intraseasonal variability and their changes in warmer climate (Andersen & Kuang, 2012; Hayashi & Sumi, 1986; Maloney et al., 2010; Maloney & Xie, 2013; also see Leroux et al., 2016, for a review).

The model and experiment design is described in section 2. Description of the MSE budget analysis and how the MSE budget is decomposed to understand the effect of climate change on the MJO are documented in section 3. A comparison of changes in MJO characteristics among simulations and discussion of

Table 1
A List of the Five Simulations and Their Average Eastward Propagation Speed in This Study

Simulation	Description	Speed (m s^{-1})
SOM_ctrl	Slab ocean simulation + "QOBS" SST Q-flux + 1×CO_2	5.65
SOM_4×CO_2	Slab ocean simulation + "QOBS" SST Q-flux + 4×CO_2	7.08
Fix_ctrl	Uncoupled simulation + mean SSTs from SOM_ctrl + 1×CO_2	5.46
Fix_4×CO_2	Uncoupled simulation + mean SSTs from SOM_ctrl + 4×CO_2	5.32
Fix_sstsom4×CO_2	Uncoupled simulation + mean SSTs from SOM_4×CO_2 + 1×CO_2	5.79

mechanisms explaining the changes in MJO propagation speed are discussed in sections 4 and 5, respectively. Conclusions and further discussion are provided in section 6.

2. Model and Experiments

All simulations were performed with the National Center for Atmospheric Research (NCAR) Community Atmosphere Model Version 5.0 (CAM5; Neale et al., 2010), which is the atmospheric component of the Community Earth System Model (CESM) Version 2.1.1. The horizontal grid spacing we use is approximately 1.9° × 2.5°, with 30 vertical levels and a 30-min time step. In CAM5, the deep and shallow convection parameterization schemes are mass flux schemes described by Zhang and McFarlane (1995) and Park and Bretherton (2009), respectively. To increase the robustness of the MJO-like signal, we doubled the entrainment rate from 1.0 to 2.0 km^{-1} in the calculation of dilute convective available potential energy (CAPE) in the deep convection scheme over the standard version, which has been documented in our previous work to substantially improve intraseasonal variability (Hannah & Maloney, 2014). We note the similar nature of the MSE budgets for entrainment rates of 1.0 and 2.0 km^{-1} in Hannah and Maloney (2014) and hence anticipate that the results shown below would exhibit limited sensitivity to the precise entrainment rate used about a value of 2.0 km^{-1}. All other physical parameterizations of the CAM5 remain unchanged. The stronger intraseasonal variability in the double entrainment rate simulation has been attributed to higher sensitivity of convection to free tropospheric humidity (Hannah & Maloney, 2014).

Our aquaplanet experiments follow the Aqua Planet Experiment (APE) protocol (Williamson et al., 2012), in which the insolation is held constant at equinoctial values, so that there is no seasonal cycle. However, a diurnal cycle is retained in insolation. All simulations are run with a zonally symmetric latitude-height distribution of ozone. The SST distribution is also zonally symmetric and varies in latitude only (Blackburn et al., 2013; Neale & Hoskins, 2000).

Since one of the foci of this study is the impact of ocean coupling on MJO change with climate warming, we conduct both prescribed SST and slab ocean model (SOM) simulations (Table 1). To do this, we first run the model with the prescribed zonally uniform and equatorially symmetric "QOBS" SST profile of Neale and Hoskins (2000):

$$T(\Phi)=\begin{cases} 27-13.5\left(\sin^2\frac{3\Phi}{2}+\sin^4\frac{3\Phi}{2}\right); -\frac{\pi}{3}\%3C\Phi\%3C\frac{\pi}{3}0°C \\ ; \text{otherwise.} \end{cases} \quad (1)$$

where Φ is latitude. From this simulation, we calculate the oceanic heat transport (Q_{flux}) for the SOM simulation that simplifies to $Q_{flux} = -F_{net}$ as described Kiehl et al. (2006), where F_{net} is the total net surface heat flux that includes instantaneous melting of snowfall reaching the surface (Benedict et al., 2017). The simulation used to compute a Q_{flux} was run for 5 years with statistics collected after the first year of integration.

The zonal mean of the Q_{flux} calculated above is then applied at every corresponding latitude in a 30 m globally uniform oceanic mixed layer depth SOM simulation. This coupled model is run for 20 years in a control simulation with historical CO_2 concentrations of 348 ppmv (SOM_ctrl hereafter) as in the Atmospheric Model Intercomparison Project (AMIP) II (Kanamitsu et al., 2002). A slab ocean simulation is also conducted with CO_2 concentrations abruptly quadrupled (SOM_4xCO_2) starting from the end of the control simulation. This perturbed simulation was run for 25 years with the last 20 years used for analysis. Global

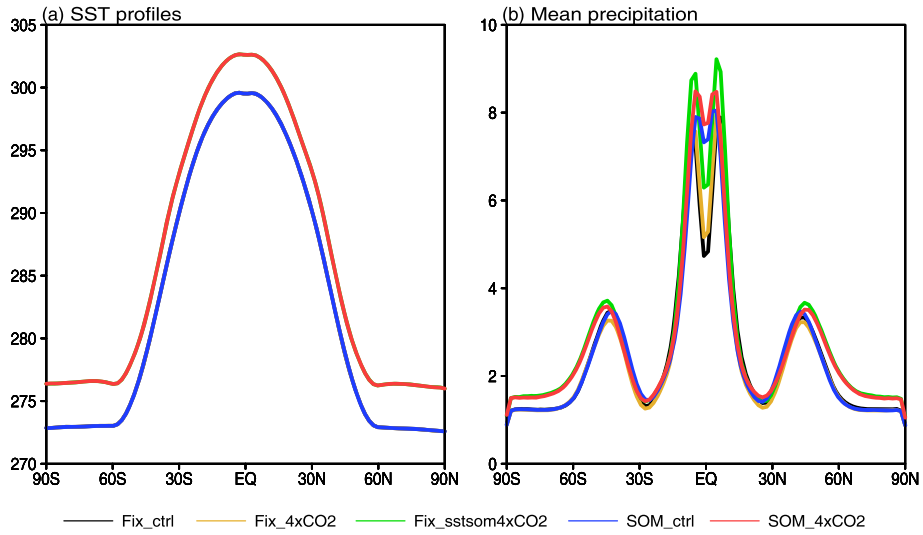

Figure 1. Zonal average of climatological mean (a) sea surface temperature (SST, units are K) and (b) mean precipitation (units are mm day^{-1}) from the five simulations described in Table 1.

mean temperature is largely stabilized by the end of the fifth year given the 30-m slab ocean depth used (not shown here). The zonal mean surface temperature from SOM_ctrl and SOM_4xCO_2 is shown in Figure 1a. Because we want to ensure an identical SST climate between uncoupled and coupled runs for the uncoupled climate change experiments described below, these SST climatologies from the coupled runs are used to force the uncoupled runs rather than starting from Equation 1. We note that the two SST profiles from the control CO_2 and the abrupt 4xCO_2 simulations with SOM show subtle differences in shape near the equator relative to the QOBS profile in Equation 1 that was used to derived Q_{flux} because of the increased rainfall and associated strong turbulent fluxes into the atmosphere produced in this region with coupling (Figure 1a, see also Klingaman & Demott, 2020). The mean precipitation patterns are characterized by a double Intertropical Convergence Zone (ITCZ) with maximum precipitation located near 10° in both hemispheres (Figure 1b). Coupled simulations have more equatorial precipitation and reduced off-equatorial precipitation than prescribed SST simulations for the same mean SST profile. Other studies have shown that even for an identical SST profile, model mean state precipitation distributions may differ substantially from model to model due to model parameterization sensitivity (e.g., Blackburn et al., 2013).

Separately examining the effect of surface temperature changes and CO_2 changes on the MJO change signal is also of interest. To determine the effect of only changing temperature, uncoupled simulations were conducted with the mean SSTs derived from the SOM_ctrl and SOM_4xCO_2 simulations (called Fix_ctrl and Fix_sstsom4xCO_2, respectively; Table 1), but with historical CO_2 concentrations. To examine the effect of only increasing CO_2 concentrations, the Fix_ctrl simulation is repeated, but with CO_2 concentrations quadrupled (Fix_4xCO_2). Each of these prescribed SST experiments was run for 20 years. Differences among simulations will be frequently examined in this paper. The differences between the Fix_4xCO_2 and Fix_ctrl experiments represent the direct effect of CO_2 concentration changes on the MJO, while the differences between Fix_sstsom4xCO_2 and Fix_ctrl provide information about the direct effect of surface warming. The differences between SOM_4xCO_2 and SOM_ctrl include combined effect from both increased CO_2 concentrations and surface warming, as mediated by ocean feedbacks. As will be seen below, the effect of CO_2 changes plus temperature changes applied separately that is derived from these fixed SST experiments does not add up to the differences between SOM_4xCO_2 and SOM_ctrl, suggesting an important role for ocean coupling in mediating the response to warming. It will be shown below that while the SST basic state changes are identical between coupled and uncoupled warming experiments, other aspects of the basic state change differently to affect the MJO response.

3. Methods

3.1. Estimation of MJO Propagation Speed

To estimate MJO propagation speed (c), we calculate an average wavenumber (k) and frequency (f) similar to the method proposed by Adames and Kim (2016). We first perform a spectral analysis in longitude for all days on the unfiltered precipitation at each latitude from 15°S to 15°N. The power spectrum (P) is then averaged for all latitudes and normalized using the formula $N(k)=\frac{P(k)}{\sum_{k=1}^{5}P(k)}$. The typical wavenumber k is obtained by summing the zonal wavenumbers from 1 to 5, weighting each one by its normalized power N. From this calculation, we obtain an average wavenumber of 2.2 for the SOM_ctrl simulation. Similar steps are applied to calculate the average frequency f, by summing across all frequencies from (1/100) to (1/20) day^{-1}. After obtaining both average zonal wavenumber and frequency, the propagation speed is simply calculated as $c = (f/k)L$, with L the Earth circumference's of 4×10^7 m (Table 1).

3.2. Moist Static Energy Budget Analysis and Decomposition

To understand the processes that regulate MJO propagation, the MJO filtered column-integrated MSE (m) budget (e.g., Maloney, 2009) is employed:

$$\left\langle \frac{\partial m}{\partial t} \right\rangle_{MJO} = -\left\langle \omega \frac{\partial m}{\partial p} \right\rangle_{MJO} - \langle \mathbf{v} \cdot \nabla m \rangle_{MJO} + LH_{MJO} + SH_{MJO} + LW_{MJO} + SW_{MJO} \tag{2}$$

where p is the pressure, $\mathbf{v}$ is the horizontal wind vector, and ω is the vertical pressure velocity. The brackets represent a mass-weighted integration through the troposphere from 1,000 to 100 hPa, and quantities with the subscript MJO represent 20- to 100-day and eastward wavenumber 1–5 filtered fields. In Equation 2, the MSE tendency, $\left\langle \frac{\partial m}{\partial t} \right\rangle$, is balanced by vertical MSE advection, $-\left\langle \omega \frac{\partial m}{\partial p} \right\rangle$, horizontal advection, $-\langle \mathbf{v} \cdot \nabla m \rangle$, and the net fluxes into the atmospheric column that include surface latent heat flux (LH), surface sensible heat flux (SH), net longwave radiation (LW), and net shortwave radiation (SW). The net radiative fluxes are calculated as the difference between the surface and top of atmosphere fluxes.

Similar to Andersen and Kuang (2012) and Wolding et al. (2016), we also project each budget quantity onto the MSE tendency to determine which terms contribute most to propagation. To do this, we calculate an area-integrated product of a budget term x and the time derivative $\langle dm/dt \rangle$, taken over all longitudes and between 10°S and 10°N, and then normalize by $\langle m \rangle^2$ to give a contribution per unit MSE:

$$T_x = \frac{\iint x \cdot \langle dm/dt \rangle dA}{\iint \langle m \rangle^2 dA} \tag{3}$$

Normalization by $\langle m \rangle^2$ provides units for Equation 3 equivalent to an inverse time scale squared and gives an indication of how strongly each term in Equation 2 can propagate an MSE anomaly. For example, if the contribution of a term increases (corresponding to decreased time scale) in a warmer climate, then this term increases the MJO's propagation speed.

In order to diagnose processes associated with horizontal MSE advection in more detail, the advection is decomposed into zonal and meridional components

$$-\langle \mathbf{v} \cdot \nabla m \rangle_{MJO} = -\left\langle u \frac{\partial m}{\partial x} \right\rangle_{MJO} - \left\langle v \frac{\partial m}{\partial y} \right\rangle_{MJO}. \tag{4}$$

The processes responsible for the regulation of zonal and meridional advection during a composite MJO event are then further examined by separating variables into their time mean component and deviation from the mean, similar to Maloney (2009). For example, u can be decomposed as $u = \overline{u} + u'$, where $\overline{u}$ represents a climatological time mean field and u' represents the deviation from $\overline{u}$. With such partitioning, the following decomposition is produced for zonal and meridional advection:

$$\left\langle u\frac{\partial m}{\partial x}\right\rangle_{MJO} \approx \left\langle \frac{u'\partial\overline{m}}{\partial x}\right\rangle_{MJO} + \left\langle \overline{u}\frac{\partial m'}{\partial x}\right\rangle_{MJO} + \left\langle u'\frac{\partial m'}{\partial x}\right\rangle_{MJO} \quad (5)$$

$$\left\langle v\frac{\partial m}{\partial y}\right\rangle_{MJO} \approx \left\langle \frac{v'\partial\overline{m}}{\partial y}\right\rangle_{MJO} + \left\langle \overline{v}\frac{\partial m'}{\partial y}\right\rangle_{MJO} + \left\langle v'\frac{\partial m'}{\partial y}\right\rangle_{MJO} \quad (6)$$

3.3. Pattern Composites

In some of the figures in this paper, we will also make use of compositing in the longitude domain to elucidate the horizontal structure of MJO-like variability. This method exploits the zonal symmetry of the SST basic state used in this study. In this procedure, we first generate a series of composite maps based on maxima of 10°N to 10°S averaged MJO filtered $\langle m\rangle$ that exceed 1σ at each longitude. A composite map is then created for each longitude that is assigned a reference longitude (0°), and fields are plotted 75° to the east and west of the reference longitude. Maps derived in a similar manner for all longitudes are then averaged to create a single map that describes the composite structure of MJO-related features. We also normalize the fields by the composite maximum value of $\langle m\rangle$ at the equator at the reference longitude of 0° to represent the tendency per unit $\langle m\rangle$ anomaly that is associated with the convective center. Note that the results shown here are not sensitive to which convective variable and threshold are used.

4. Basic Characteristics of the Response

Before presenting detailed simulation intercomparisons, wavenumber-frequency spectra of equatorial (15°S to 15°N averaged) precipitation are examined from the five simulations (Figure 2). The Fix_ctrl simulation is characterized by a strong peak at wavenumber 1 and about 60 days (Figure 2a). The uncoupled simulation with abruptly quadrupled CO_2 concentration and fixed control SST shows a modest reduction in spectral power at eastward intraseasonal periods as compared to the Fix_ctrl simulation (Figure 2c), implying a small negative direct contribution of CO_2 increases to MJO precipitation amplitude. Previous studies have argued that increasing CO_2 concentrations in the atmosphere can produce a rapid increase in atmospheric stability due to the direct impact of radiative forcing, reducing convection and precipitation (Yang et al., 2003). Similar behavior at the intraseasonal time scale might be manifest here, although the changes are small and likely not significant. Conversely, the uncoupled simulation with control CO_2 concentration levels and mean SST taken from the SOM_4xCO_2 simulation shows a notable increase in variance at Zonal wavenumbers 1 to 3 relative to Fix_ctrl that expands to higher frequencies (Figure 2d). This feature suggests a stronger and faster MJO with surface warming, consistent with other studies (e.g., Adames et al., 2017; Arnold et al., 2013; Chang et al., 2015; Cui & Li, 2019; Rushley et al., 2019). We note that in addition to the wavenumber-frequency spectra analysis shown above, we also assessed propagation speed changes using Hovmoller diagrams derived from lag regression onto an Indian Ocean base point and found a similar result (Figure S4 in the supporting information).

For the SOM simulations, the control run shows a variance peak with maximum concentrated near a frequency of (1/50) day^{-1} (Figure 2b), consistent with observed MJO spectral characteristics (Waliser et al., 2009). The coupled simulation (SOM_ctrl) indicates faster propagation than the corresponding uncoupled simulation with identical mean SST (Fix_ctrl), consistent with the results of DeMott et al. (2019), although the difference in propagation speed indicated in Table 1 is not statistically significant. The SOM_4xCO_2 spectrum increases in amplitude with the variance maximum shifting to higher frequencies relative to SOM_ctrl (Figure 2e), consistent with results from previous studies (e.g., Maloney et al., 2019). The frequency shift in the variance maximum is greater than for Fix_sstsom4xCO_2, despite the identical mean state SST changes between the simulations. This result suggests that the effect of ocean coupling leads to greater increases in MJO propagation speed in a warmer climate compared to uncoupled simulations, a result that might be anticipated given the tendency for ocean coupling to enhance MJO propagation speed relative to uncoupled simulations in the current climate (see Table 1 and DeMott et al., 2019). However, we also show below that differing basic state wind changes between the coupled and uncoupled runs may help to mediate the response in ways not anticipated by DeMott et al. (2019), in which coupling modified meridional moisture gradients to influence MJO propagation speed. Summing the effect of CO_2 changes and temperature changes derived from the two fixed SST experiments does not reproduce the difference

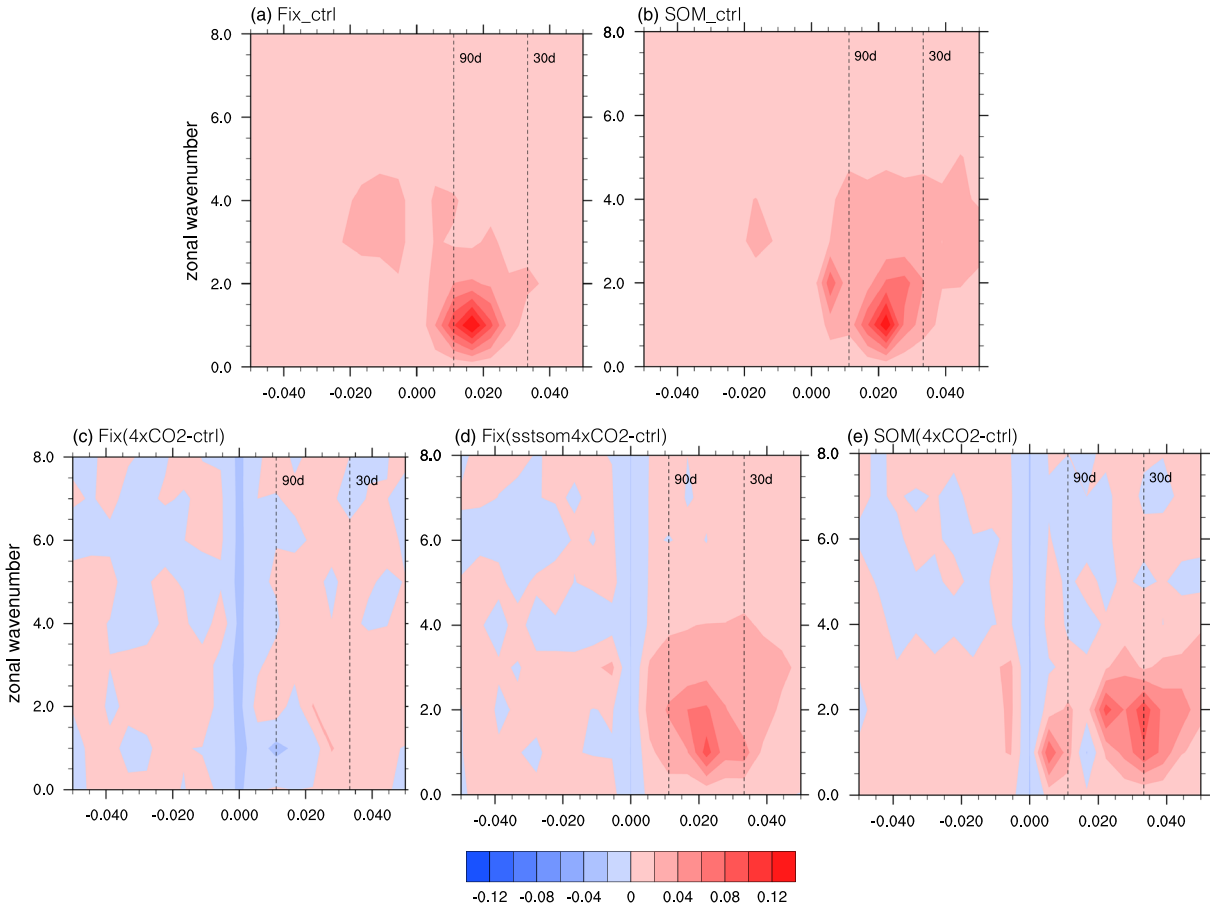

Figure 2. Wavenumber-frequency spectra of model equatorial (15°S to 15°N averaged) precipitation from (a) Fix_ctrl, (b) SOM_ctrl, (c) Fix_4xCO_2 minus Fix_ctrl, (d) Fix_sstsom4xCO_2 minus Fix_ctrl, and (e) SOM_4xCO_2 minus SOM_ctrl. Units are $mm^2\ day^{-2}$.

between SOM_4xCO_2 and SOM_ctrl (figure not shown), further highlighting that coupling is important for mediating the response to warming.

Figure 3 shows the fractional change of the MJO frequency, wavenumber, and phase speed relative to the control simulations (i.e., Fix_ctrl and SOM_ctrl). For example, the fractional change of propagation speed (c) in Fix_4xCO_2 relative to Fix_ctrl is calculated as $(c_{\text{Fix\_4xCO2}} - c_{\text{Fix\_ctrl}})/c_{\text{Fix\_ctrl}}$. With increases in 4x$CO_2$ concentrations and SSTs from Fix_ctrl, both frequency and wavenumber changes are relatively small, resulting a small change in the MJO propagation speed (cf. Fix_4xCO_2 and Fix_ctrl). This supports the finding that the direct effects of CO_2 increase only produce modest effects on MJO characteristics. In contrast, with the CO_2 concentration held fixed at preindustrial levels but the SST increased, MJO propagation speed increases. MJO propagation speed is increased most strongly in the coupled experiments with SST warming induced by CO_2 increases, associated with increased frequency and reduced wavenumber. The reduction of zonal wavenumber in our SOM simulations is consistent with that found in fully coupled CMIP5 models (e.g., Rushley et al., 2019), suggesting that MJO horizontal scale will become larger in a future warmer climate (Adames et al., 2017). The reasons for differences in eastward propagation speed between coupled and uncoupled simulations will be further examined in the next section.

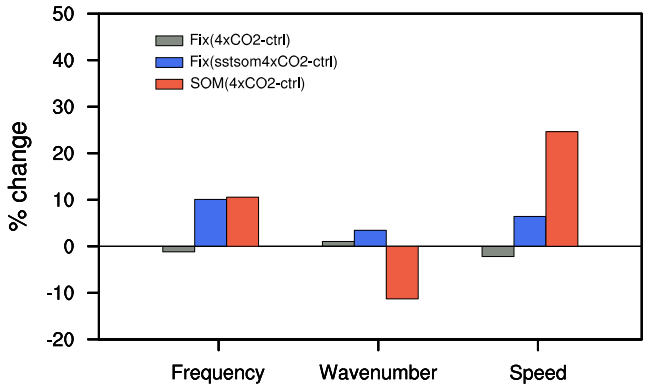

Figure 3. Fractional change of MJO frequency, wavenumber, and propagation speed among simulations as calculated in section 3.1. Units are %.

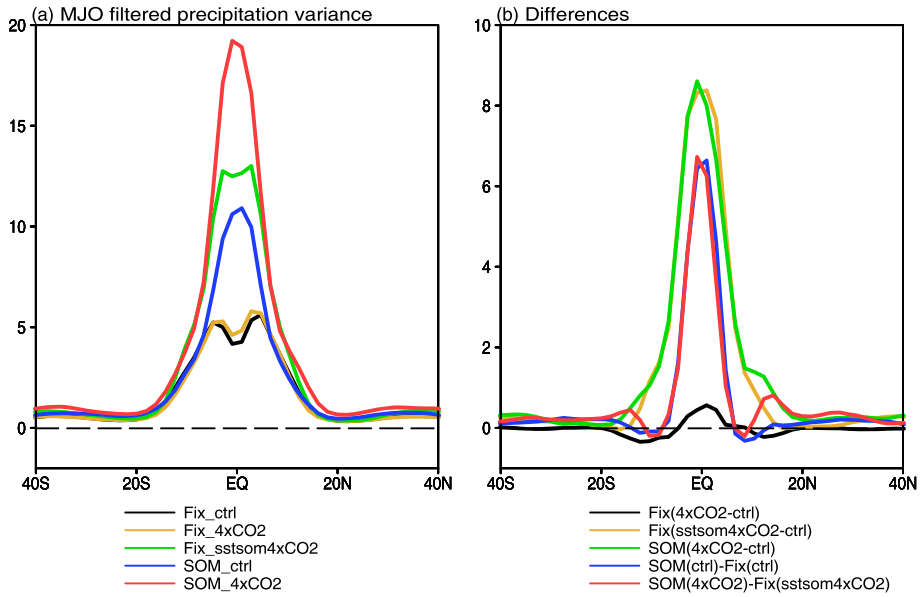

Figure 4. Zonal average of MJO filtered precipitation variance from (a) the five simulations and (b) differences among simulations. Units are $mm^2\ day^{-2}$.

To better quantify the amplitude of MJO changes under $4xCO_2$, Figure 4 shows the zonal average of the 20- to 100-day and eastward wavenumber 1–5 filtered precipitation variance. For all simulations, MJO precipitation is highest near the equator, although coupled experiments have a stronger equatorial maximum. SST warming is associated with stronger precipitation variance (Figure 4a). A close examination of Figures 1b and 4a (after translating Figure 4a to a standard deviation) indicates that MJO time and space scale precipitation variability increases at a noticeably greater rate with warming than mean precipitation for all the simulations. Hence, the increase in MJO precipitation variability cannot be simply explained by an increase in total precipitation. The differences are brought out more strongly in Figure 4b. The quadrupled CO_2 simulation with fixed control SST demonstrates very modest negative changes in precipitation variance (black curve in Figure 4b). Conversely, simulations with increased surface temperature exhibit an increase in MJO precipitation variance generally where precipitation variance was already high in the corresponding control simulation (orange and green curves in Figure 4b). The differences between coupled and uncoupled simulations with the same mean SST imply the effect of the ocean feedbacks (blue and red curves in Figure 4b). Stronger MJO precipitation is produced near the equator with coupling when compared to uncoupled simulations with the same mean SST. Interestingly, the stronger MJO precipitation that is produced in SOM_$4xCO_2$ appears to support stronger equatorial superrotation, consistent with the results of Carlson and Caballero (2016). Figure S1 featuring the equatorial zonal wind climatology shows that not only is stronger superrotation supported in the coupled run with warming, but lower and middle tropospheric zonal winds are less easterly. Both of these changes may help support faster eastward MJO propagation with warming in the coupled versus uncoupled runs, as explained below.

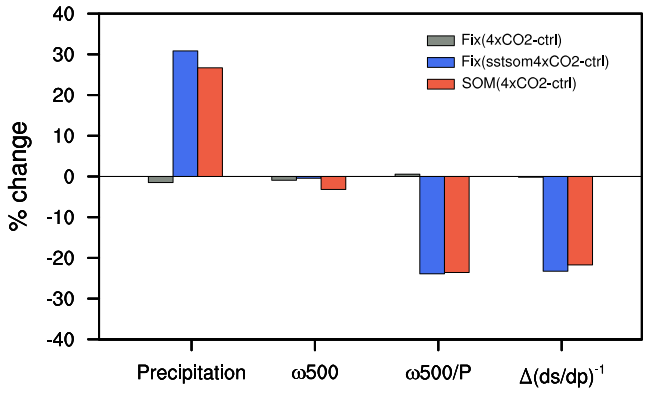

Figure 5. Fractional change in the standard deviation of MJO filtered precipitation, 500-hPa pressure velocity (omega), the ratio between the two, and the change in the static stability (vertical dry static energy gradient averaged from 400 to 500 hPa) averaged over the tropics (20°S to 20°N). Units are %.

Changes in the MJO circulation with warming in previous modeling studies were shown to be related to the changes in MJO precipitation through increased tropical static stability (Bui & Maloney, 2018; Maloney & Xie, 2013). Figure 5 shows the fractional change in the MJO amplitude (defined as the standard deviation of MJO filtered fields) of precipitation, 500-hPa pressure velocity, and the ratio of pressure velocity and precipitation averaged over the tropics (20°S

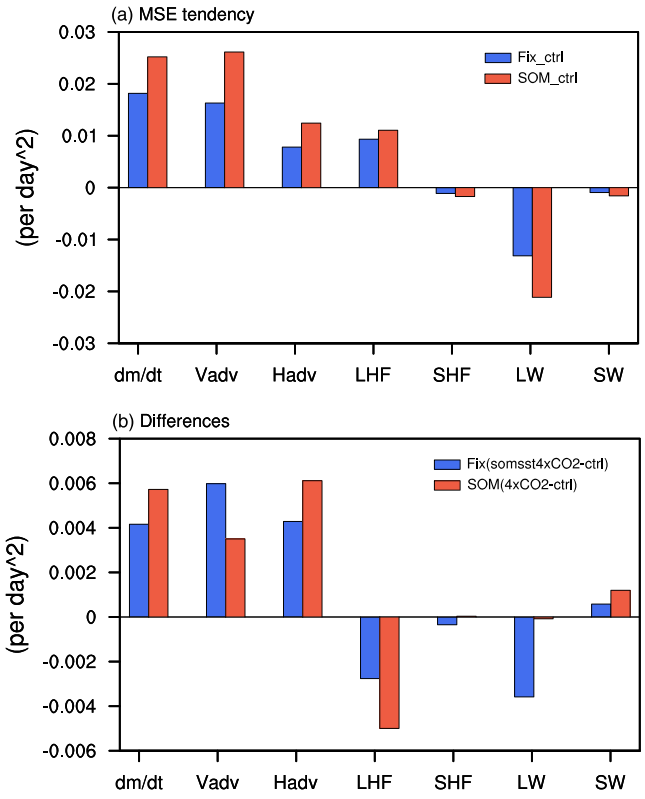

Figure 6. (a) Contribution of each MSE budget term to the MSE tendency (dm/dt) averaged over the tropics (10°S to 10°N) in the Fix_ctrl and SOM_ctrl simulations and (b) differences between simulations. Units are day^{-2}.

to 20°N). Increasing CO_2 concentrations alone produces a very small and insignificant negative change to MJO precipitation and wind amplitudes. However, MJO precipitation anomaly amplitude increases while associated circulations change little with surface warming in both coupled and uncoupled simulations, consistent with previous studies (e.g., Bui & Maloney, 2018). Following Bui and Maloney (2019b), the change in ratio of MJO circulation to precipitation anomalies is also examined. The ratio is reduced in both coupled and uncoupled simulation with surface temperature warming, consistent with tropical static stability increases with warming (Bui & Maloney, 2019b). A similar result is also found for the ratio of 850-hPa zonal wind amplitude to precipitation (not shown). A reduction in MJO wind anomaly per unit precipitation would have consequences for MJO propagation, since wind anomalies for the same strength precipitation anomaly would be reduced relative to a cooler control simulation (e.g., Adames & Kim, 2016).

Because of the very small direct impacts of increased CO_2 concentrations on MJO change, we will not explore this issue further and will instead focus hereafter on how surface warming and the effect of coupling influence MJO change. The MSE budget will be used to diagnose the mechanisms responsible for changes in MJO propagation speed.

5. Mechanisms for the MJO Propagation Speed Changes

Figure 6a shows the contribution of the various MSE budget terms to the normalized MSE tendency per unit MSE anomaly, which we hypothesize to be proportional to the MJO propagation speed, in the coupled and uncoupled control simulations. Related frameworks have been used in other studies to diagnose processes responsible for MJO propagation speed (Andersen & Kuang, 2012; Wolding et al., 2016). As a reminder, these terms were calculated using Equations 2 and 3. Given the construction of the variance budget, only the contribution of the various tendency terms to supporting the anomalous MSE tendency of the MJO are captured by this analysis. Vertical advection, Vadv, is the dominant source (sink) of MSE tendency to the east (west) of the convection center, contributing to eastward propagation. Note that Vadv peaks on the equator, consistent with previous studies of DeMott et al. (2016) and Wolding et al. (2016) who show that frictional convergence through vertical advection is a major mechanism for eastward propagation (see Figure 8d for the spatial distribution that includes radiative heating). The horizontal advection, Hadv, also fosters eastward propagation in the control simulations (Figure 6a). These contributions are most strongly manifest eastward and poleward of the convective center at reference longitude 0° (Figure 8a). The surface latent heat flux, LHF (Figure S2a), also contributes to eastward propagation of the MJO, consistent with the aquaplanet results of Andersen and Kuang (2012). We note that surface fluxes are slightly larger in the coupled versus uncoupled simulation, implying a role for ocean feedbacks in modulating surface fluxes. However, the wind-driven part of the flux anomaly is dominant in the MJO and hence we would not expect large changes in the flux contribution to the tendency between coupled and uncoupled models (e.g., DeMott et al., 2019). Because we are using a zonally symmetric model with mean surface easterlies, the phase relationship between surface LHF anomalies and MJO convection is likely different than the real world where the MJO exists in regions of mean surface westerlies and surface fluxes peak to the west of MJO convection (Maloney et al., 2010; Zhang & McPhaden, 2000). Longwave radiation anomalies, LW, caused primarily by fluctuations in high clouds slow the eastward propagation in the control experiments (see also Figure S2d). The other terms—the sensible heat flux (SHF) and shortwave radiation (SW)—produce only modest contributions to the MSE tendency.

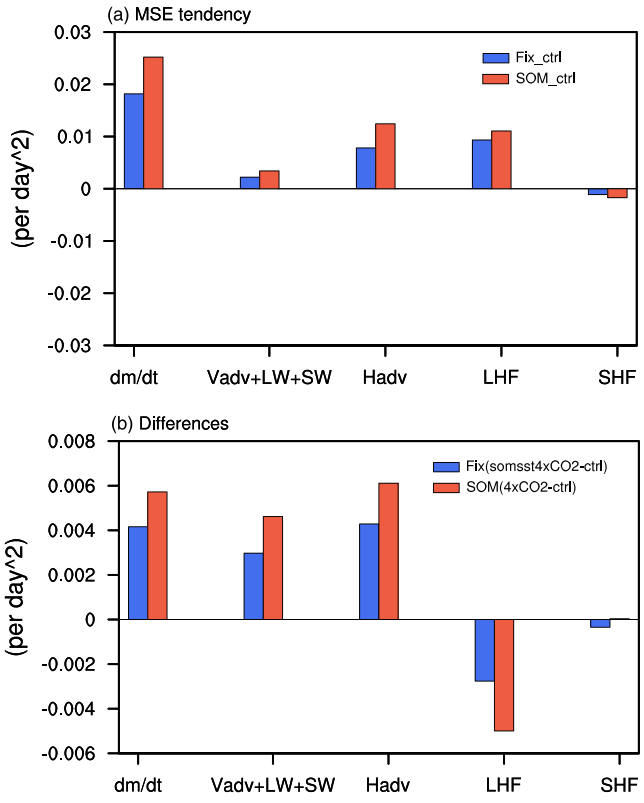

Figure 7. As in Figure 6 except vertical advection and radiative heating are combined into one term to represent the column process.

Differences with warming between coupled and uncoupled simulations are shown in Figure 6b. The fractional changes of MSE tendency are positive and greater in the coupled model relative to the uncoupled one, consistent with greater MJO propagation speed change in previous section (see Figure 3). Both horizontal and vertical advection make positive contributions to the MSE tendency changes, thus favoring faster eastward propagation. In both coupled and uncoupled models, the surface LHF anomalies have a negative contribution to the MSE tendency change, thus wanting to slow the MJO in a warmer climate. The weakened surface LHF feedback may be due to the weakened dynamical response to MJO per unit precipitation as the surface flux anomaly is strongly dependent on the low-level MJO wind and wind speed anomalies (cf. change in MJO wind in Figure 5). This is in agreement with previous studies that have shown LHF anomalies change in such a way to slow eastward propagation in a warmer climate (e.g., Arnold et al., 2015; Wolding et al., 2017). However, we note that in these previous studies the model produced LHF anomalies that maximize to the east of the MJO in warm pool regions, opposite to what is observed. Hence, our results and those of Arnold et al. (2015) and Wolding et al. (2017) should be viewed with caution when assessing the impacts of flux changes with warming on MJO propagation. Other MSE terms show small or negative contributions to the MSE tendency change, except for a moderate contribution from longwave radiation in the uncoupled simulations.

While the sign of the change in MSE budget terms with warming is generally similar between the coupled and uncoupled runs, the explanation for why the total tendency change is greater with coupling is complex. LW anomalies appear to become a stronger drag on eastward propagation in the uncoupled run relative to the coupled run (Figures 6b and S2e). Combined with weaker mean upper tropospheric westerly winds in the uncoupled run (Figure S1), the stronger weakening of anomalous upper level circulations to the east of 0° longitude (not shown) may support reduced advection of cloud condensate to the east of the MJO convective center in the uncoupled run versus the coupled run, preferentially raising outgoing longwave radiation (OLR) there and reducing column radiative heating (Figure S2b). As discussed in previous studies (e.g., Chikira, 2014; Wolding et al., 2016), examining radiative heating in isolation from the vertical advection term is misleading in capturing the full influence of radiative heating on the MJO's moisture evolution. Radiative heating anomalies are balanced by upward motion through weak temperature gradient balance (Adames & Kim, 2016; Sobel & Maloney, 2013), and hence, part of the effect of radiative heating is captured in the vertical advection term. Hence, it is appropriate to add the effects of radiative heating together with vertical advection to diagnose their effect on MJO moistening, into a term that has previously been termed the column process (Janiga & Zhang, 2016; Wolding et al., 2016). Figure 7 shows that both the column process and horizontal advection contribute to faster eastward propagation in the coupled run versus the uncoupled run. The change in the radiative anomaly is important to understanding why the MJO speeds up more in the coupled versus uncoupled run. Figure S5 indicates increased descent with warming to the east of MJO convection in the uncoupled run versus coupled run that is presumably consistent with this effect. Figure 7a also shows that once radiative heating is combined with vertical advection, horizontal advection, and LHF become dominant regulators of eastward propagation in the control models.

Given the important contribution of horizontal and the sum of vertical advection and radiative anomalies to the increased MJO propagation speed, composite maps of these two terms presented together with MSE tendency anomalies and low-level surface wind anomalies help elucidate the mechanisms responsible for the increase in eastward propagation speed with warming. Composite horizontal advection normalized by the $\langle m \rangle$ was first examined in the SOM_ctrl simulation (Figure 8a). Recall that we normalize by the strength of the peak $\langle m \rangle$ anomaly (i.e., at reference longitude 0° where precipitation peaks) to give a sense for how

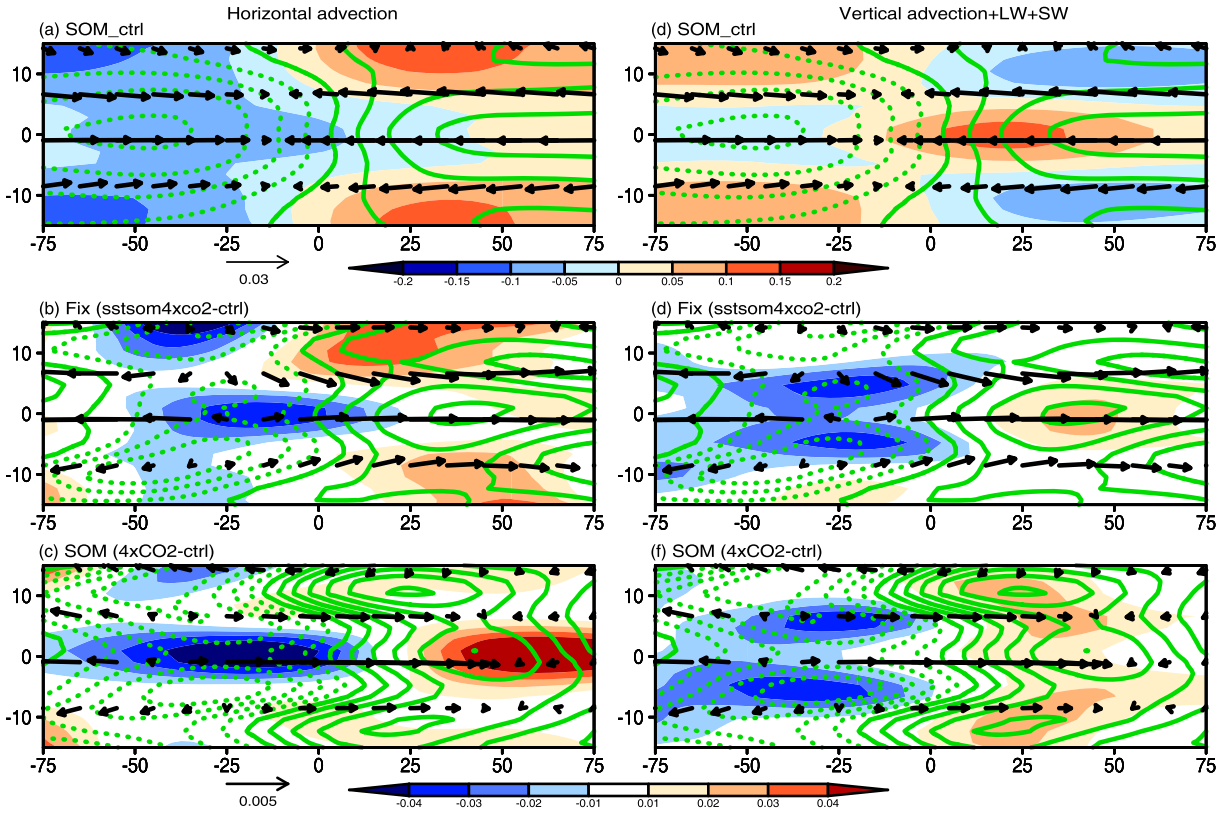

Figure 8. (a) Composite (see detail description in section 3.3) column-integrated horizontal MSE advection anomalies (shaded, see color scale below the panel), MSE tendency (contour) and 850-hPa vector wind anomalies, and differences between the (b) uncoupled simulations (Fix_sstsom4xCO_2 minus Fix_ctrl) and (c) coupled simulations (SOM_4xCO_2 minus SOM_ctrl). The contour interval is 0.03 interval for the SOM_ctrl and at 0.005 interval for the difference plots. Solid contours are positive. Units are day^{-1}. (d–f) As in (a)–(c) except for the sum of vertical MSE advection and radiative heating anomalies.

rapidly a tendency term is able to propagate the $\langle m \rangle$ anomaly. A positive (negative) anomaly of horizontal advection (shaded) occurs to the east (west) of the convective center, consistent with the positive (negative) MSE tendency anomalies (in contours) and anomalous low-level easterly (westerly) winds (in vectors), similar to the results from previous studies who showed a large and positive horizontal advection anomaly to the east of peak precipitation (e.g., Kiranmayi & Maloney, 2011; Maloney, 2009). This positive anomaly to the east and drying pattern near and to the west of enhanced MJO convection would foster eastward propagation of the MSE and corresponding convection anomaly through moisture mode theory (e.g., Chikira, 2014; Chikira & Sugiyama, 2013; Maloney et al., 2010; Sugiyama, 2009).

We next examine changes in coupled and uncoupled simulations under surface temperature warming relative to their respective control simulations (Figures 8b and 8c). In horizontal advection, the coupled simulation shows different behavior from the uncoupled experiment, with positive tendency changes accentuated at the equator to the east of the MSE maximum at 0° (Figure 8c), consistent with the larger increase shown in Figure 7b. In general, changes of horizontal advection show a pattern consistent to that of changes in MSE tendency anomalies, suggesting its crucial role in speeding up the MJO propagation speed in a warmer climate, consistent with Figure 6 and many previous studies (e.g., Adames et al., 2017; Rushley et al., 2019). We note that this horizontal advection change with warming is generally out of phase with surface LHF change (Figure S2), but with a larger amplitude.

Similarly, Figures 8d–8f show the composite patterns of the vertical MSE advection plus radiative heating (column process) anomalies and their changes with warming. The column process projects positively onto the MSE tendency pattern, making it important for eastward propagation (Figure 8d). With warming, changes in vertical advection plus radiation enhance the zonal asymmetry of MSE tendency per unit MSE anomaly—more positive (negative) anomalies to the east (west) of the MSE and convective center,

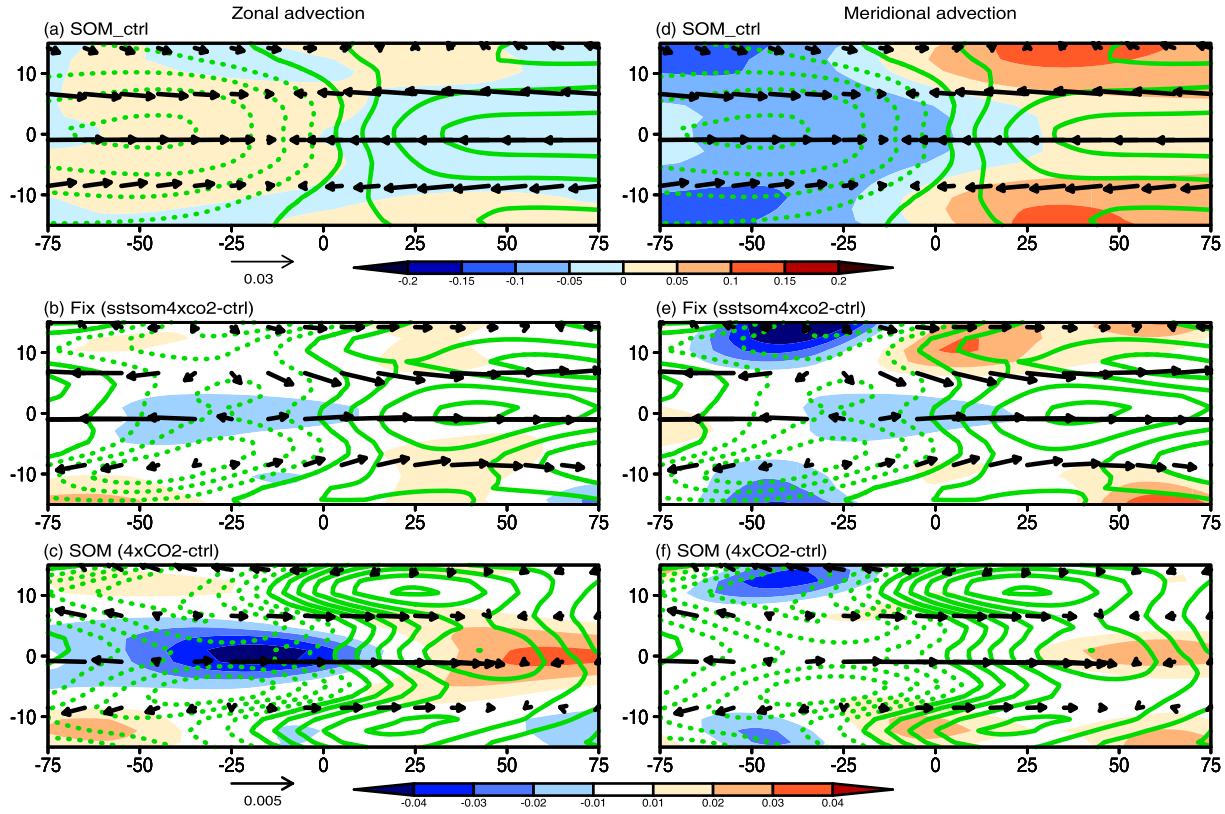

Figure 9. As in Figure 8 except that the shaded fields are (a–c) zonal and (d–f) meridional MSE advection components.

favoring faster eastward propagation. Comparison between coupled and uncoupled models based on this plot is not straightforward, although the total tendency change when averaged from 10°N to 10°S to the east of MJO convection is greatest in the coupled simulation, consistent with Figure 7b (not shown here). The off-equatorial negative radiative heating anomaly change in the uncoupled simulation to the east of MJO convection (Figure S2) appears to reduce the latitudinal expanse of the positive column process change in that model (Figure 8e).

The above analyses conclude that horizontal advection is an important factor contributing to faster MJO propagation in a warmer climate in both coupled and uncoupled models. To further understand how horizontal advection affects MJO propagation speed change with warming, the term is partitioned into zonal and meridional components (Figure 9). In the control SOM simulation, the meridional component tends to be more similar to the total horizontal advection anomaly than the zonal component (cf. Figures 9a and 9d). However, with warming, the change the zonal component appears comparably important as the meridional term to the total horizontal advection change. Note that the drying effect of zonal advection to the east of convective center is reduced in both uncoupled and coupled models, with a stronger reduction in the latter, suggesting that this would lead to a faster eastward propagation based on moisture mode theory. A particularly prominent change in zonal advection is found in the coupled simulation on the equator that does not exist in the uncoupled simulation.

We further decompose variables that constitute the advection terms into a time mean component and deviation from the time mean as prescribed by Equations 5 and 6. Figure 10 is generated as the same way as Figure 6, which is the projection/contribution of the partitioned zonal and meridional components to the normalized MSE tendency per unit MSE anomaly. As shown in Figure 10a for the coupled and uncoupled control simulations, total zonal advection is dominated by the mean zonal flow across the perturbation MSE gradient, $\left\langle \overline{u}\frac{\partial m'}{\partial x} \right\rangle_{MJO}$, and partially canceled by the term $\left\langle u'\frac{\partial m'}{\partial x} \right\rangle_{MJO}$. Note that the term $\left\langle \frac{u'\partial \overline{m}}{\partial x} \right\rangle_{MJO}$ is almost zero because of the zonal symmetry of SST basic state pattern. The total meridional

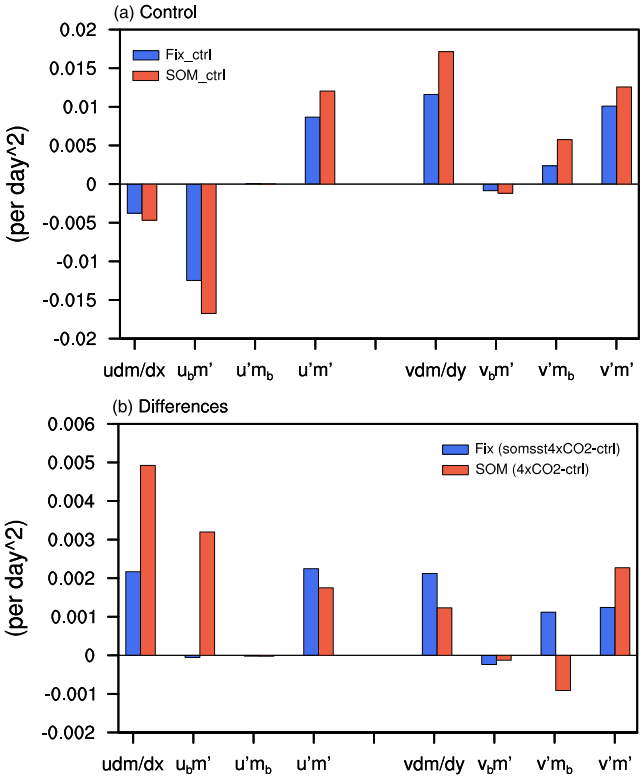

Figure 10. Same as Figure 6 except for the contribution from zonal and meridional advection and their time decomposition described in Equations 5 and 6. Shown are the contribution due to the advection of anomalous MSE by the mean zonal wind ($u_b m'$) and mean meridional wind ($v_b m'$), advection of mean MSE by the anomalous zonal wind ($u' m_b$) and anomalous meridional wind ($v' m_b$), and advection of anomalous MSE by the anomalous zonal wind ($u' m'$), and anomalous meridional wind ($v' m'$).

advection in both coupled and uncoupled simulations is positive and dominated by $\left\langle v' \frac{\partial m'}{\partial y} \right\rangle_{MJO}$, suggesting the important of synoptic eddies in regulating the intraseasonal MSE budget, consistent with Maloney (2009), although this effect may be overestimated in the model compared to that in observations (e.g., Kim et al., 2014). The contributions from other meridional terms are nonnegligible but are of smaller amplitude.

In a warmer climate, a notable increase in the term $\left\langle \overline{u} \frac{\partial m'}{\partial x} \right\rangle_{MJO}$ occurs in the coupled simulation (Figure 10b), suggesting an important contribution from weakening of the lower tropospheric easterly mean zonal wind to speed-up of the MJO in the coupled run relative to the uncoupled run. Figure S1 shows that lower and middle tropospheric mean easterly winds are preferentially weakened in the coupled run with warming, with such changes preferentially occurring on the equator (not shown), consistent with the pattern of zonal advection change in Figures 8c and 9c. The change in the zonal basic state clearly explains the increased zonal advection in the coupled run in Figure 10, thus contributing to speeding up the MJO. The reduction of lower tropospheric mean easterlies on the equator is consistent with that found in Carlson and Caballero (2016) for simulations with stronger superrotation (their Figure 5). Differences in meridional advection with warming for the coupled and uncoupled runs, while not small, are not as prominent as for zonal advection. Interestingly, the change in $\left\langle \frac{v' \partial \overline{m}}{\partial y} \right\rangle_{MJO}$ is not consistent between coupled and uncoupled simulations, which is somewhat unexpected given that previous studies have found warming produces a stronger meridional moisture gradient near the equator and faster eastward propagation (e.g., Adames et al., 2017). The mean meridional MSE gradient in the simulations is generally complex (Figure S3a), making its role in MJO propagation complicated. The meridional moisture gradient increases more strongly with warming from 10°N to 10°S in the uncoupled run (Figure S3b), consistent with Figure 10b. The maps in Figure 11 show little coherent structure to the change in $\left\langle \frac{v' \partial \overline{m}}{\partial y} \right\rangle_{MJO}$ for the coupled and uncoupled experiments. Weakening of the MJO circulation consistent with tropical static stability increases would opposes any strengthening of the meridional humidity gradient in the context of changes to the term $\left\langle \frac{v' \partial \overline{m}}{\partial y} \right\rangle_{MJO}$ (Adames et al., 2017; Maloney & Xie, 2013). Figure 10 also suggests the effect of eddies on advection becomes stronger in a warmer climate in both the coupled and uncoupled runs. However, the pattern of the advection change due to eddies is difficult to interpret (not shown), and requires future work to understand the dynamics.

Finally, we show the composite pattern of the terms $\left\langle \overline{u} \frac{\partial m'}{\partial x} \right\rangle_{MJO}$ and $\left\langle \frac{v' \partial \overline{m}}{\partial y} \right\rangle_{MJO}$ to help better understand the controlling factor for the change of MJO propagation speed. Consistent with Figure 10b, the term $\left\langle \overline{u} \frac{\partial m'}{\partial x} \right\rangle_{MJO}$ shows a significant increase to the east of the convective center with a strong equatorial signature in the coupled simulation (Figure 11c), suggesting that weaker mean easterly winds in the coupled simulation are speeding up the MJO with warming. A coherent pattern of change in $\left\langle \frac{v' \partial \overline{m}}{\partial y} \right\rangle_{MJO}$ is difficult to discern in both the uncoupled and uncoupled experiments, consistent with the discussion in the previous paragraph.

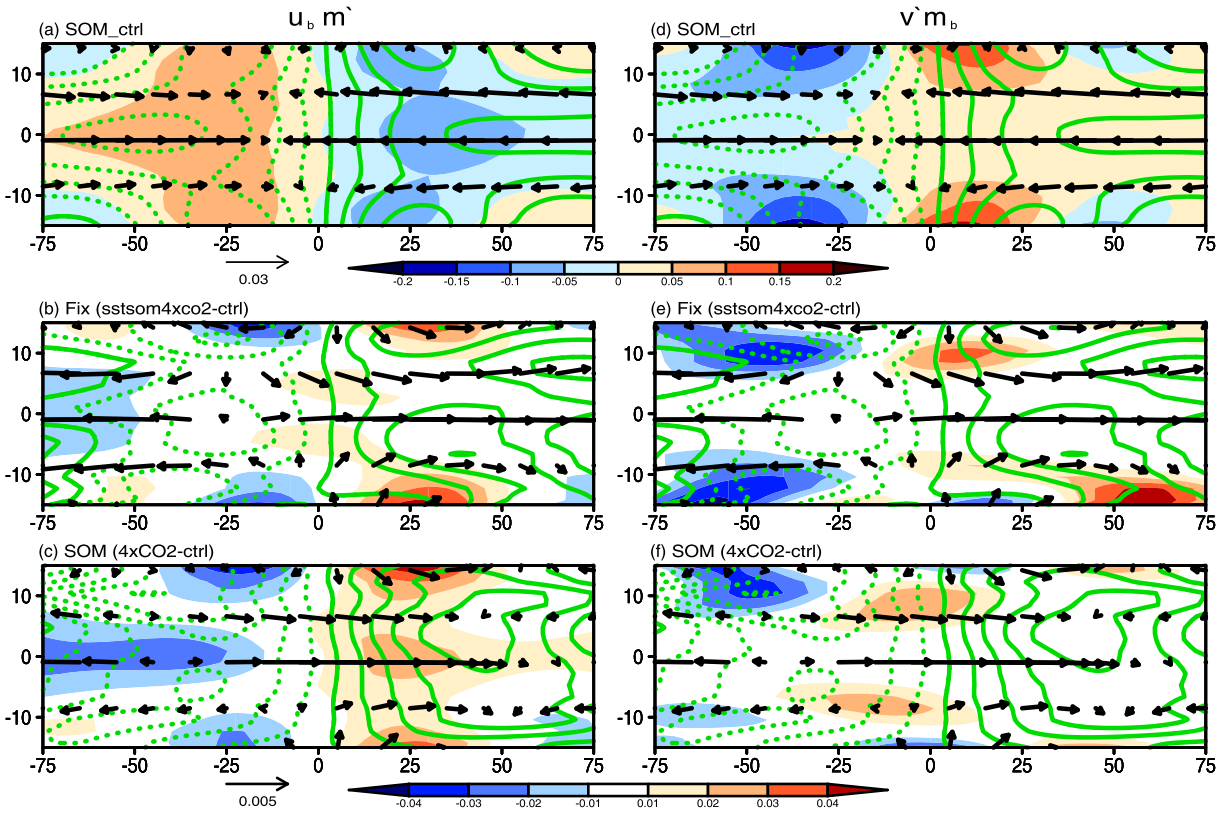

Figure 11. As in Figure 8 except for the contribution due to (a–c) advection of perturbation MSE by the mean zonal wind flow and (d–f) advection of mean MSE by the anomalous meridional wind flow.

6. Summary and Discussion

In this study, we quantified how much MJO changes in a future climate depend directly upon on increased CO_2 concentrations versus surface warming and investigated how ocean coupling affects the MJO response to warming. Our results show that (1) quadrupling CO_2 concentrations have only a small and insignificant impact on the MJO characteristics when surface temperature is held fixed. Temperature changes arising from quadrupling of CO_2 produces a substantial increase in MJO precipitation variability, a slower increase in MJO circulation variability, and faster MJO eastward propagation. (2) Ocean coupling is associated with greater increases in MJO propagation speed than in an uncoupled model, even for the same mean SST climatology.

The increases in MJO precipitation amplitude with warming, weaker circulations per unit precipitation, and faster eastward propagation speed shown here are consistent with that found in previous studies (e.g., Adames et al., 2017; Arnold et al., 2013, 2015; Bui & Maloney, 2018, 2019a; Maloney et al., 2019; Rushley et al., 2019; Wang & Li, 2020). However, a new result here is that coupled experiments produce a greater speed-up in MJO propagation speed with warming than uncoupled experiments in which the same magnitude and pattern of warming is applied. An analysis of the MSE budget diagnoses some possible reasons for this disparate behavior. The coupled experiments are associated with stronger MJO variability with warming than uncoupled experiments, which appears to lead to stronger equatorial superrotation than in the uncoupled model. The associated stronger mean westerlies aloft and weaker lower and middle tropospheric mean easterlies in the coupled model both weaken the drying effects of zonal advection by the mean easterly wind to the east of MJO convection and also affect the strength of radiative heating anomalies to the east of MJO advection, presumably by modifying advection of cloud condensate to the east of the MJO convective center. This latter effect is more uncertain and requires exploration with further model sensitivity testing. While faster MJO propagation speeds in a

warmer climate with coupling were not totally unexpected, the mechanism was. DeMott et al. (2019) emphasized the importance of coupling for increasing the mean state column water vapor near the equator, thus favoring faster MJO propagation in current climate runs relative to uncoupled models. However, meridional humidity gradients strengthen more in the uncoupled model with warming relative to coupled experiments (Figure S3). Admittedly, the aquaplanet configuration and the climate model used here are not as realistic as that in DeMott et al. (2019), who used the SP-CESM. Hence, our experiments deserve to be repeated with a more sophisticated modeling setup.

In general, the current results are based on idealized experiments that do not resemble the real world in many important ways. Thus, we hesitate to extrapolate our results to predict how future MJO activity may change with warming in the real climate system. Regardless, robust conclusions of our study are that coupled and uncoupled models produce different changes to MJO characteristics, even if the SST climatologies are identical, and that increased CO_2 concentrations do not appear to have any important direct impacts on the MJO in the absence of surface temperature changes. The precise mechanisms underlying the differences between coupled and uncoupled responses of the MJO to warming shown here require further study.

Data Availability Statement

Data from all simulations analyzed in this paper can be obtained at the website (https://doi.org/10.25675/10217/205828).

Acknowledgments
We thank Jim Benedict for useful discussion about running the aquaplanet model. This work was supported by the Climate and Large-Scale Dynamics Program of the National Science Foundation under Grant AGS-1841754. We would like to acknowledge high-performance computing support from Cheyenne (doi:10.5065/D6RX99HX) provided by NCAR's Computational and Information Systems Laboratory, sponsored by the National Science Foundation.

References

Adames, Á. F., & Kim, D. (2016). The MJO as a dispersive, convectively coupled moisture wave: Theory and observations. *Journal of the Atmospheric Sciences*, *73*(3), 913–941. https://doi.org/10.1175/JAS-D-15-0170.1

Adames, Á. F., Kim, D., Sobel, A. H., Del Genio, A., & Wu, J. (2017). Changes in the structure and propagation of the MJO with increasing CO_2. *Journal of Advances in Modeling Earth Systems*, *9*, 1251–1268. http://doi.org/10.1002/2017MS000913

Andersen, J. A., & Kuang, Z. (2012). Moist static energy budget of MJO-like disturbances in the atmosphere of a zonally symmetric aquaplanet. *Journal of Climate*, *25*(8), 2782–2804. https://doi.org/10.1175/JCLI-D-11-00168.1

Araligidad, N. M., & Maloney, E. D. (2008). Wind-driven latent heat flux and the intraseasonal oscillation. *Geophysical Research Letters*, *35*, L04815. https://doi.org/10.1029/2007GL032746

Arnold, N. P., Branson, M., Kuang, Z., Randall, D. A., & Tziperman, E. (2015). MJO intensification with warming in the superparameterized CESM. *Journal of Climate*, *28*(7), 2706–2724. https://doi.org/10.1175/JCLI-D-14-00494.1

Arnold, N. P., Kuang, Z., & Tziperman, E. (2013). Enhanced MJO-like variability at high SST. *Journal of Climate*, *26*(3), 988–1001. https://doi.org/10.1175/JCLI-D-12-00272.1

Benedict, J. J., Medeiros, B., Clement, A. C., & Pendergrass, A. G. (2017). Sensitivities of the hydrologic cycle to model physics, grid resolution, and ocean type in the aquaplanet Community Atmosphere Model. *Journal of Advances in Modeling Earth Systems*, *9*, 1307–1324. https://doi.org/10.1002/2016MS000891

Bessafi, M., & Wheeler, M. C. (2006). Modulation of South Indian Ocean tropical cyclones by the Madden–Julian Oscillation and convectively coupled equatorial waves. *Monthly Weather Review*, *134*, 638–656. https://doi.org/10.1175/MWR3087.1

Blackburn, M., & Hoskins, B. J. (2013). Context and aims of the Aqua-Planet Experiment. *Journal of the Meteorological Society of Japan Series II*, *91*, 1–15. https://doi.org/10.2151/jmsj.2013-A01

Blackburn, M., Williamson, D. L., Nakajima, K., Ohfuchi, W., Takahashi, Y. O., Hayashi, Y.-Y., et al. (2013). The Aqua-Planet Experiment (APE): CONTROL SST simulation. *Journal of the Meteorological Society of Japan Series II*, *91A*, 17–56. https://doi.org/10.2151/jmsj.2013-A02

Bony, S., Bellon, G., Klocke, D., Sherwood, S., Fermepin, S., & Denvil, S. (2013). Robust direct effect of carbon dioxide on tropical circulation and regional precipitation. *Nature Geoscience*, *6*(6), 447–451. https://doi.org/10.1038/ngeo1799

Bui, H. X., & Maloney, E. D. (2018). Changes in Madden-Julian Oscillation precipitation and wind variance under global warming. *Geophysical Research Letters*, *45*, 7148–7155. https://doi.org/10.1029/2018GL078504

Bui, H. X., & Maloney, E. D. (2019a). Mechanisms for global warming impacts on Madden-Julian Oscillation precipitation amplitude. *Journal of Climate*, *32*, 6961–6975. https://doi.org/10.1175/JCLI-D-19-0051.1

Bui, H. X., & Maloney, E. D. (2019b). Transient response of MJO precipitation and circulation to greenhouse gas forcing. *Geophysical Research Letters*, *46*, 13,546–13,555. https://doi.org/10.1029/2019GL085328

Carlson, H., & Caballero, R. (2016). Enhanced MJO and transition to superrotation in warm climates. *Journal of Advances in Modeling Earth Systems*, *8*, 304–318. https://doi.org/10.1002/2015MS000615

Chang, C.-W. J., Tseng, W.-L., Hsu, H.-H., Keenlyside, N., & Tsuang, B.-J. (2015). The Madden-Julian Oscillation in a warmer world. *Geophysical Research Letters*, *42*, 6034–6042. https://doi.org/10.1002/2015GL065095

Chikira, M. (2014). Eastward-propagating intraseasonal oscillation represented by Chikira-Sugiyama cumulus parameterization. Part II: Understanding moisture variation under weak temperature gradient balance. *Journal of the Atmospheric Sciences*, *71*(2), 615–639. https://doi.org/10.1175/JAS-D-13-038.1

Chikira, M., & Sugiyama, M. (2013). Eastward-propagating intraseasonal oscillation represented by Chikira–Sugiyama cumulus parameterization. Part I: Comparison with observation and reanalysis. *Journal of the Atmospheric Sciences*, *70*(12), 3920–3939. https://doi.org/10.1175/JAS-D-13-034.1

Cui, J., & Li, T. (2019). Changes of MJO propagation characteristics under global warming. *Climate Dynamics*, *53*(9-10), 5311–5327. https://doi.org/10.1007/s00382-019-04864-4

DeMott, C. A., Benedict, J. J., Klingaman, N. P., Woolnough, S. J., & Randall, D. A. (2016). Diagnosing ocean feedbacks to the MJO: SST-modulated surface fluxes and the moist static energy budget. *Journal of Geophysical Research: Atmospheres*, *121*, 8350–8373. https://doi.org/10.1002/2016JD025098

DeMott, C. A., Klingaman, N. P., Tseng, W.-L., Burt, M. A., Gao, Y., & Randall, D. A. (2019). The convection connection: How ocean feedbacks affect tropical mean moisture and MJO propagation. *Journal of Geophysical Research: Atmospheres*, *124*, 11,910–11,931. https://doi.org/10.1029/2019JD031015

DeMott, C. A., Klingaman, N. P., & Woolnough, S. J. (2015). Atmosphere-ocean coupled processes in the Madden-Julian oscillation. *Reviews of Geophysics*, *53*, 1099–1154. https://doi.org/10.1002/2014RG000478

DeMott, C. A., Stan, C., Randall, D. A., & Branson, M. D. (2014). Intraseasonal variability in coupled GCMs: The roles of ocean feedbacks and model physics. *Journal of Climate*, *27*(13), 4970–4995. https://doi.org/10.1175/JCLI-D-13-00760.1

Fu, J.-X., Wang, W., Shinoda, T., Ren, H.-L., & Jia, X. (2017). Toward understanding the diverse impacts of air-sea interactions on MJO simulations. *Journal of Geophysical Research: Oceans*, *122*, 8855–8875. https://doi.org/10.1002/2017JC013187

Fu, X., Wang, W. Q., Lee, J.-Y., Kikuchi, K., Xu, J. W., Li, J., & Weaver, S. (2015). Distinctive roles of air-sea coupling on different MJO events: A new perspective revealed from the DYNAMO/CINDY field campaign. *Monthly Weather Review*, *143*, 794–812. https://doi.org/10.1175/MWR-D-14-00221.1

Gonzalez, A. O., & Jiang, X. (2017). Winter mean lower-tropospheric moisture over the Maritime Continent as a climate model diagnostic metric for the propagation of the Madden-Julian Oscillation. *Geophysical Research Letters*, *44*, 2588–2596. https://doi.org/10.1002/2016GL072430

Gregory, J., & Webb, M. (2008). Tropospheric adjustment induces a cloud component in CO_2 forcing. *Journal of Climate*, *21*(1), 58–71. https://doi.org/10.1175/2007JCLI1834.1

Grimm, A. M. (2019). Madden–Julian Oscillation impacts on South American summer monsoon season: Precipitation anomalies, extreme events, teleconnections, and role in the MJO cycle. *Climate Dynamics*, *53*(1-2), 907–932. https://doi.org/10.1007/s00382-019-04622-6

Hannah, W. M., & Maloney, E. D. (2014). The moist static energy budget in NCAR CAM5 hindcasts during DYNAMO. *Journal of Advances in Modeling Earth Systems*, *6*, 420–440. https://doi.org/10.1002/2013MS000272

Hayashi, Y. Y., & Sumi, A. (1986). The 30-40 day oscillations simulated in an "aqua planet" model. *Journal of the Meteorological Society of Japan Series II*, *64*(4), 451–467. https://doi.org/10.2151/jmsj1965.64.4_451

Henderson, S. A., Maloney, E. D., & Barnes, E. A. (2016). The influence of the Madden-Julian oscillation on Northern Hemisphere winter blocking. *Journal of Climate*, *29*(12), 4597–4616. https://doi.org/10.1175/JCLI-D-15-0502.1

Henderson, S. A., Maloney, E. D., & Son, S.-W. (2017). Madden-Julian oscillation Pacific teleconnections: The impact of the basic state and MJO representation in general circulation models. *Journal of Climate*, *30*(12), 4567–4587. https://doi.org/10.1175/JCLI-D-16-0789.1

Hendon, H. H. (2000). Impact of air-sea coupling on the Madden-Julian Oscillation in a general circulation model. *Journal of the Atmospheric Sciences*, *57*, 3939–3952. https://doi.org/10.1175/1520-0469(2001)058%3C3939:IOASCO%3E2.0.CO;2

Janiga, M. A., & Zhang, C. (2016). MJO moisture budget during DYNAMO in a cloud-resolving model. *Journal of the Atmospheric Sciences*, *73*(6), 2257–2278. https://doi.org/10.1175/JAS-D-14-0379.1

Jiang, X. (2017). Key processes for the eastward propagation of the Madden-Julian Oscillation based on multimodel simulations. *Journal of Geophysical Research: Atmospheres*, *122*, 755–770. https://doi.org/10.1002/2016JD025955

Kanamitsu, M., Ebisuzaki, W., Woollen, J., Yang, S. K., Hnilo, J. J., Fiorino, M., & Potter, G. L. (2002). NCEP–DOE AMIP-II Reanalysis (R-2). *Bulletin of the American Meteorological Society*, *83*(11), 1631–1644. https://doi.org/10.1175/BAMS-83-11-1631

Kiehl, J. T., Shields, C. A., Hack, J. J., & Collins, W. D. (2006). The climate sensitivity of the Community Climate System Model Version 3 (CCSM3). *Journal of Climate*, *19*(11), 2584–2596. https://doi.org/10.1175/JCLI3747.1

Kim, D., Kug, J.-S., & Sobel, A. H. (2014). Propagating versus non-propagating Madden-Julian oscillation events. *Journal of Climate*, *27*(1), 111–125. https://doi.org/10.1175/JCLI-D-13-00084.1

Kim, D., Sperber, K., Stern, W., Waliser, D., Kang, I. S., Maloney, E., & Lee, M. I. (2009). Application of MJO simulation diagnostics to climate models. *Journal of Climate*, *22*(23), 6413–6436. https://doi.org/10.1175/2009JCLI3063.1

Kiranmayi, L., & Maloney, E. D. (2011). Intraseasonal moist static energy budget in reanalysis data. *Journal of Geophysical Research*, *116*, D21117. https://doi.org/10.1029/2011JD016031

Klingaman, N. P., & Demott, C. A. (2020). Mean state biases and interannual variability affect perceived sensitivities of the Madden-Julian Oscillation to air-sea coupling. *Journal of Advances in Modeling Earth Systems*, *12*, e2019MS001799. https://doi.org/10.1029/2019MS001799

Klingaman, N. P., & Woolnough, S. J. (2014). The role of air-sea coupling in the simulation of the Madden-Julian Oscillation in the Hadley Centre model. *Quarterly Journal of the Royal Meteorological Society*, *140*(684), 2272–2286. https://doi.org/10.1002/qj.2295

Klotzbach, P. J., & Oliver, E. C. J. (2015). Modulation of Atlantic basin tropical cyclone activity by the Madden-Julian Oscillation (MJO) from 1905 to 2011. *Journal of Climate*, *28*, 204–217. https://doi.org/10.1175/JCLI-D-14-00509.1

Leroux, S., Bellon, G., Roehrig, R., Caian, M., Klingaman, N. P., Lafore, J.-P., et al. (2016). Inter-model comparison of subseasonal tropical variability in aquaplanet experiments: Effect of a warm pool. *Journal of Advances in Modeling Earth Systems*, *8*, 1526–1551. https://doi.org/10.1002/2016MS000683

Madden, R. A., & Julian, P. R. (1971). Detection of a 40–50 day oscillation in the zonal wind in the tropical Pacific. *Journal of the Atmospheric Sciences*, *28*(5), 702–708. https://doi.org/10.1175/1520-0469(1971)028%3C0702:DOADOI%3E2.0.CO;2

Madden, R. A., & Julian, P. R. (1972). Description of global-scale circulation cells in the tropics with a 40–50 day period. *Journal of the Atmospheric Sciences*, *29*(6), 1109–1123. https://doi.org/10.1175/1520-0469(1972)029%3C1109:DOGSCC%3E2.0.CO;2

Maloney, E. D. (2009). The moist static energy budget of a composite tropical intraseasonal oscillation in a climate model. *Journal of Climate*, *22*, 711–729. https://doi.org/10.1175/2008JCLI2542.1

Maloney, E. D., Adames, Á. F., & Bui, H. X. (2019). Madden-Julian oscillation changes under anthropogenic warming. *Nature Climate Change*, *9*(1), 26–33. https://doi.org/10.1038/s41558-018-0331-6

Maloney, E. D., & Hartmann, D. L. (2000). Modulation of hurricane activity in the Gulf of Mexico by the Madden-Julian oscillation. *Science*, *287*(5460), 2002–2004. https://doi.org/10.1126/science.287.5460.2002

Maloney, E. D., & Sobel, A. H. (2004). Surface fluxes and ocean coupling in the tropical intraseasonal oscillation. *Journal of Climate*, *17*(22), 4368–4386. https://doi.org/10.1175/JCLI-3212.1

Maloney, E. D., Sobel, A. H., & Hannah, W. M. (2010). Intraseasonal variability in an aquaplanet general circulation model. *Journal of Advances in Modeling Earth Systems*, *2*, 5. https://doi.org/10.3894/JAMES.2010.2.5

Maloney, E. D., & Xie, S.-P. (2013). Sensitivity of tropical intraseasonal variability to the pattern of climate warming. *Journal of Advances in Modeling Earth Systems*, *5*(1), 32–47. https://doi.org/10.1029/2012MS000171

Marshall, A. G., & Hendon, H. H. (2015). Subseasonal prediction of Australian summer monsoon anomalies. *Geophysical Research Letters*, *42*, 10–913. https://doi.org/10.1002/2015GL067086

Mitchell, J. F. (1983). The seasonal response of a general circulation model to changes in CO_2 and sea temperatures. *Quarterly Journal of the Royal Meteorological Society*, *109*(459), 113–152. https://doi.org/10.1002/qj.49710945906

Neale, R. B., Chen, C., Gettelman, A., Lauritzen, P., Park, S., Williamson, D., et al. (2010). Description of the NCAR community atmosphere model (CAM 5.0). *NCAR Tech. Note NCAR/TN-486+ STR*.

Neale, R. B., & Hoskins, B. J. (2000). A standard test for AGCMs including their physical parametrizations: I: The proposal. *Atmospheric Science Letters*, *1*(2), 101–107. https://doi.org/10.1006/asle.2000.0022

Park, S., & Bretherton, C. S. (2009). The University of Washington shallow convection and moist turbulence schemes and their impact on climate simulations with the Community Atmosphere Model. *Journal of Climate*, *22*(12), 3449–3469. https://doi.org/10.1175/2008JCLI2557.1

Raymond, D. J., & Fuchs, Ž. (2009). Moisture modes and the Madden–Julian oscillation. *Journal of Climate*, *22*(11), 3031–3046. https://doi.org/10.1175/2008JCLI2739.1

Riley Dellaripa, E. M., & Maloney, E. D. (2015). Analysis of MJO wind-flux feedbacks in the Indian Ocean using RAMA buoy observations. *Journal of the Meteorological Society of Japan Series II*, *93A*, 1–20. https://doi.org/10.2151/jmsj.2015-021

Rushley, S. S., Kim, D., & Adames, Á. F. (2019). Changes in the MJO under greenhouse gas-induced warming in CMIP5 models. *Journal of Climate*, *32*(3), 803–821. https://doi.org/10.1175/JCLI-D-18-0437.1

Sobel, A., & Maloney, E. (2013). Moisture modes and the eastward propagation of the MJO. *Journal of the Atmospheric Sciences*, *70*(1), 187–192. https://doi.org/10.1175/JAS-D-12-0189.1

Sobel, A. H., & Maloney, E. D. (2000). Effect of ENSO and the MJO on western North Pacific tropical cyclones. *Geophysical Research Letters*, *27*(12), 1739–1742. https://doi.org/10.1029/1999GL011043

Sobel, A. H., Maloney, E. D., Bellon, G., & Frierson, D. M. (2008). The role of surface heat fluxes in tropical intraseasonal oscillations. *Nature Geoscience*, *1*(10), 653–657. https://doi.org/10.1038/ngeo312

Sugiyama, M. (2009). The moisture mode in the quasi-equilibrium tropical circulation model. Part I: Analysis based on the weak temperature gradient approximation. *Journal of the Atmospheric Sciences*, *66*(6), 1507–1523. https://doi.org/10.1175/2008JAS2690.1

Vitart, F. (2009). Impact of the Madden Julian Oscillation on tropical storms and risk of landfall in the ECMWF forecast system. *Geophysical Research Letters*, *36*, L15802. https://doi.org/10.1029/2009GL039089

Vitart, F. (2014). Evolution of ECMWF sub-seasonal forecast skill scores. *Quarterly Journal of the Royal Meteorological Society*, *140*(683), 1889–1899. https://doi.org/10.1002/qj.2256

Waliser, D. E., Murtugudde, R., & Lucas, L. E. (2003). Indo-Pacific Ocean response to atmospheric intraseasonal variability: 1. Austral summer and the Madden-Julian Oscillation. *Journal of Geophysical Research*, *108*(C5), 3160. https://doi.org/10.1029/2002JC001620

Waliser, D. E., Sperber, K., Hendon, H., Kim, D., Maloney, E., & Wheeler, M. (2009). MJO simulation diagnostics. *Journal of Climate*, *22*(11), 3006–3030. https://doi.org/10.1175/2008JCLI2731.1

Wang, B., Chen, G., & Liu, F. (2019). Diversity of the Madden-Julian oscillation. *Science Advances*, *5*, eaax0220. https://doi.org/10.1126/sciadv.aax0220

Wang, L., & Li, T. (2020). Effect of vertical moist static energy advection on MJO eastward propagation: Sensitivity to analysis domain. *Climate Dynamics*, *54*(3-4), 2029–2039. https://doi.org/10.1007/s00382-019-05101-8

Wheeler, M. C., Hendon, H. H., Cleland, S., Meinke, H., & Donald, A. (2009). Impacts of the Madden–Julian oscillation on Australian rainfall and circulation. *Journal of Climate*, *22*(6), 1482–1498. https://doi.org/10.1175/2008JCLI2595.1

Williamson, D. L., Blackburn, M., Hoskins, B. J., Nakajima, K., Ohfuchi, W., Takahashi, Y. O., et al. (2012). The APE atlas (Technical Report 10.5065/D6FF3QBR). National Center for Atmospheric Research. https://doi.org/10.5065/D6FF3QBR

Wolding, B. O., Maloney, E. D., & Branson, M. (2016). Vertically resolved weak temperature gradient analysis of the Madden-Julian Oscillation in SP-CESM. *Journal of Advances in Modeling Earth Systems*, *8*, 1586–1619. https://doi.org/10.1002/2016MS000724

Wolding, B. O., Maloney, E. D., Henderson, S., & Branson, M. (2017). Climate change and the Madden-Julian Oscillation: A vertically resolved weak temperature gradient analysis. *Journal of Advances in Modeling Earth Systems*, *9*, 307–331. https://doi.org/10.1002/2016MS000843

Yang, F., Kumar, A., Schlesinger, M. E., & Wang, W. (2003). Intensity of hydrological cycles in warmer climates. *Journal of Climate*, *16*(14), 2419–2423. https://doi.org/10.1175/2779.1

Zhang, C. (2005). Madden-Julian Oscillation. *Reviews of Geophysics*, *43*, RG2003. https://doi.org/10.1029/2004RG000158

Zhang, C., & Gottschalck, J. (2002). SST anomalies of ENSO and the Madden–Julian oscillation in the equatorial Pacific. *Journal of Climate*, *15*(17), 2429–2445. https://doi.org/10.1175/1520-0442(2002)015%3C2429:SAOEAT%3E2.0.CO;2

Zhang, C., & McPhaden, M. J. (2000). Intraseasonal surface cooling in the equatorial western Pacific. *Journal of Climate*, *13*, 2261–2276. https://doi.org/10.1175/1520-0442(2000)013%3C2261:ISCITE%3E2.0.CO;2

Zhang, G., & McFarlane, N. A. (1995). Sensitivity of climate simulations to the parameterization of cumulus convection in the Canadian climate Centre general circulation model. *Atmosphere-Ocean*, *33*(3), 407–446. https://doi.org/10.1080/07055900.1995.9649539